A macro-scale approach to computational fluid dynamics modelling of the reduction of manganese ore by hydrogen

by M.I. Khama[1], Q.G. Reynolds[1,2], B.S. Xakalashe[1]

Affiliation:
[1]Mintek, Randburg, South Africa
[2]University of Stellenbosch, Department of Chemical Engineering, Matieland, South Africa

Correspondence to:
M.I. Khama

Email:
mopelik@mintek.co.za

Dates:
Received: 9 Sept. 2024
Accepted: 12 Nov. 2024
Published: March 2025

How to cite:
Khama, M.I., Reynolds, Q.G., Xakalashe, B.S. 2025. A macro-scale approach to computational fluid dynamics modelling of the reduction of manganese ore by hydrogen. *Journal of the Southern African Institute of Mining and Metallurgy*, vol. 125, no. 3, pp. 151–160

DOI ID:
https://doi.org/10.17159/2411-9717/3559/2025

ORCiD:
M.I. Khama
http://orcid.org/0000-0003-1443-6262
Q.G. Reynolds
http://orcid.org/0000-0002-5196-8586
B.S. Xakalashe
http://orcid.org/0000-0003-0069-7082

Abstract

The carbonaceous reduction of manganese ore is an energy-intensive process that releases large amounts of pollutant gases. In an attempt to circumvent the greenhouse gas emissions, this research investigates hydrogen as an alternative reductant. The reduction of manganese ore with hydrogen results in the structural changes in the intermediate products, which might limit the diffusion of the reactant gases through the pores. Computational fluid dynamics (CFD) models capture the structural changes and predict the rate controlling mechanism and this is key in designing the prereduction reactors. The current work uses CFD models to predict the degree of reduction in a shaft furnace under hydrogen reducing conditions. Manganese ore is described as a collection of scalar and tensor fields such as thermal conductivity of the porous medium, density, and viscous resistance. The results indicate that advection contributes significantly towards the overall transport of hydrogen to the reaction sites. Porosity of the final product was found to be higher than porosity of the raw material.

Keywords

CFD, diffusion limitations, kinetic limitations, solid-state reduction, hydrogen

Introduction

The production of high carbon ferromanganese is achieved through the reduction of manganese ore in a submerged arc furnace (SAF) and utilises carbon as a reductant. The process is energy-intensive and this is particularly evident in carbonate rich manganese ores. This is because the thermal decomposition of carbonates is highly endothermic, and this increases the energy requirements. However, some furnace operations charge manganese sinter in the electric furnace resulting in the reduction of the smelting energy consumption (Liu et al., 2024). This is because manganese sinter does not have carbonates as they decompose during sintering. In cases where sinter is not used, the high-energy requirements coupled with high greenhouse gas emissions necessitated a need to explore alternative reductants. Several researchers have investigated the solid-state reduction using H_2 as a potential reductant for prereduction (Patisson et al., 2020; Wu et al., 2024; Ma et al. 2022). Prereduction offers advantages such as reduced energy consumption in the downstream smelting. Furthermore, prereduction of carbonate rich manganese ores by H_2 results in the acceleration of the carbonate decomposition (Davies et al., 2023).

The reduction behavior of manganese ores is non-uniform since manganese ores contain minerals with different compositions of manganese and iron (Coetsee et al., 2015). The heterogeneous nature of manganese ores requires that the reaction mechanism and kinetic data for each ore be determined before process equipment design. In the context of solid-state prereduction of manganese ore with H_2, a shaft furnace can be used, and the kinetic parameters are key for the design and upscale of the shaft furnace.

The prereduction of manganese lumps or pellets with H_2 in a shaft furnace represents a reacting flow problem that is susceptible to mass transfer limitations. However, H_2 has a small molecular size and diffuses easily into the ore. The diffusion of H_2 happens through three mechanisms namely, physisorption, chemisorption, and H_2 uptake (Li et al., 2024). Physisorption happens due to the Van der Waals forces between H_2 and the manganese ore surface and is influenced by temperature and pressure. Chemisorption concerns the formation of covalent bond between molecules (Christmann, 1988). H_2 uptake involves incorporation of H_2 into the metal oxide lattice structure through desorption.

The knowledge of reaction mechanism in the pre-reduction of manganese ores with H_2 is crucial. Owing to the importance of understanding the kinetics and reaction mechanism for prereduction

with H_2, Rukini et al. (2022) carried out some studies aimed at understanding this phenomenon. These researchers state that lattice oxygen in the oxide is removed, and the process is driven by H_2O removal. The diffusion of H_2 into the metal oxide structure, which results in the breaking of metal oxide bonds is facilitated by the transformation of molecular H_2 into atomic state (Kung, 1989). Upon breaking the metal oxide bonds, the formation of a hydroxyl group and metal hydride follows. The resultant metal hydride is volatile and subsequently releases H_2 to form H_2O with hydroxyl followed by water vapour desorption (Rukini et al., 2022).

The chemical reactions might be fast enough to facilitate the desired reduction and conversion, however, the transport of H_2 from the bulk gas phase to the reaction sites affects the reaction concentration. Therefore, the reduction kinetics are strongly coupled with heat and mass transfer and a numerical model needs to capture this phenomenon. This is particularly evident in the solid-state reduction of a packed bed of pellets in a shaft furnace (Hamadeh et al., 2018). It is vital to characterise several performance indicators of industrial heterogeneous reactors in order to gauge the optimum operating conditions. However, the performance of industrial heterogeneous reactions at high temperatures is difficult to measure during the operation. This shortcoming is addressed by using the CFD models, which are able to capture the dynamic features of industrial heterogeneous processes. The fixed bed reactor performance and productivity is influenced by the gas-solid reactions, therefore, the development of robust, coupled reaction kinetics and transport models is of paramount importance.

Several researchers have developed reaction models for gas-solid reactions (Hamadeh et al., 2018; Li et al, 2023; Kinaci et al., 2020). These models include the shrinking core model and the grain model. The shrinking core model works for simplified cases and its applicability is confined to cases where the inward diffusion controls the reaction (Ahn et al., 2017). In most cases, the heterogeneous reaction system constitutes a multi-step and multi-species process, and this renders the shrinking core model unsuitable. This is because the condition of multiple reaction steps and equilibrium reactions, among other factors, result in model deviations (Wesenauer et al., 2020). A more accurate reaction modelling approach is the one that considers the pellet as a porous spherical agglomerate of composite grains. The robustness and generality of such a model can manifest in its predictive capability of pre-reduction behavior of a bed of pellets or lumps in a shaft furnace.

A shaft furnace is by design a complex reactor that involves multiphase flows coupled with high temperature and pressure. It is crucial to measure parameters that influence the process performance. However, it is difficult to measure them during operation. Numerical models that consider multiphase flows and couple chemical kinetics with transport phenomena circumvent these shortcomings. An example of such a model is a shaft furnace model developed by Li et al. (2023), which uses the well-established volume-averaged multiphase Navier Stokes equations to describe the gas phase in a reacting gas-solid system. The authors assumed a steady state and considered the momentum, mass, and energy conservation for the two phases. Their continuum-based model was validated against performance indicators measured from plant operation based on production using H_2 and natural gas.

The gas-solid dynamics in a shaft furnace can be captured through modelling approaches such as Eulerian two-phase models, plug flow models, direct numerical simulation (DNS), and computational fluid dynamics and discrete element methods (CFD-DEM). DNS does not require closure models, and its predictions result in the highest resolution of gas and particle flow. However, it is computationally expensive and limited to low Reynolds numbers and a finite number of fluid elements, rendering it unsuitable for most real applications. CFD-DEM model is able to capture the particle descent and flow patterns in a furnace due to its ability to account for drag force (Fei et al., 2024). The larger number of particles in the furnace coupled with longer spatial and temporal scales including non-linear equations impose high computational expense on CFD-DEM models. The plug flow models are unable to resolve the particles and assume a constant axial velocity and this allows for faster evaluation of gas-solid flow in industrial shaft furnaces. Given the high computational expense of CFD-DEM and DNS models and inaccuracy of plug flow models, further research is needed to develop computationally efficient and accurate heterogeneous reacting flow models.

Liu et al. (2023) developed a 3D CFD model to investigate the influence of reducing gas temperature on physical quantities in a shaft furnace with the view to optimise the operating conditions. Their model assumes that the moving bed of pellets has uniform porosity and ignores the interaction between particles in the furnace charge. The heat transfer between gas and solid phase considers convection and chemical reaction heat. In the cases where the reactions take place at high temperatures, the effects of radiative heat transfer are significant and have to be included in the energy equation.

The current work utilises the CFD reacting flow models developed by Jan Źuk et al. (2022) to investigate the reduction behaviour of manganese ore under H_2 in a shaft furnace. The approach utilises a standalone CFD solver that couples fluid flow, heat transfer, and heterogeneous reactions in a porous medium. The geometry of the porous medium is taken into account by its physical characteristics. The inclusion of ore particles into the computational domain is done by using the special form of the immersed boundary method named the fictitious domain (Jan Źuk et al.,2022). In this study, the porous medium in the fictitious domain is defined by its physical characteristics that include scalar porosity and tensor viscous resistance. As mentioned above, the models used to predict the gas-solid dynamics are computationally expensive. However, the current approach is an efficient and easy implementation that allows for rapid numerical computation, particularly for cases where there is need to change the physical characteristics of the geometry or flow during calculation time without remeshing the domain and rewriting the corresponding boundary conditions. The study considers a fixed bed of particles with uniform porosity, and predicts the species mass fractions and the structural changes as the products are formed from gas-solid reactions.

Numerical model

A bed of particles as depicted in Figure 1, is described by its physical properties that include density, thermal conductivity, and porosity. The CFD model developed by Jan Źuk et al. (2022) represents the porous medium as a volume field within a computational domain. To simplify the implementation, the porous medium is assumed to be either entirely inside or outside the computational cell. This is done to minimise the need to use two or more computational cells to resolve porous medium.

The gas flow through the porous medium is integrated with heterogeneous reactions. In the heterogeneous reactions where there is a possibility of mass transfer limitations, the CFD model must incorporate the effects of diffusion limitations. In this study, Damkohler number (Da_i) is used to determine whether the reaction

rates are controlled by diffusion or chemical reactions. Dai is defined by the ratio of characteristic diffusion time to characteristic surface reaction time as depicted in Equation 1.

$$Da_i = \frac{\tau_{diffusion,i}}{\tau_{chemical\ reaction,i}} \quad [1]$$

In the diffusion-controlled regime, $Da_i \rightarrow \infty$ because in this case, diffusion is slower than the reaction at the surface, whereas in the chemical reaction-controlled regime, $Da_i \rightarrow 0$ since the reactions at the surface are slower than diffusion. The other way to gauge the operating regime is to evaluate the ratio of diffusion flux to reaction rate flux. The diffusion flux is calculated from Fick's law and the reaction rate based on species diffusion is modelled according to Equation 2:

$$R_s^{diff} = K_g S_{AV} \rho^G \left(Y_i^G - Y_i^s\right) \quad [2]$$

Where Kg (m/s) is mass transfer coefficient, S_{AV} (m^{-1}) is the ratio of surface area to volume, R^{dif}_s (kg m^{-3} s^{-1}) is the volume averaged reaction rate, ρ^G (kg m^{-3}) is the fluid density, Y_i^G is the bulk mass fraction of the reduction gas, and Y_i^S is the surface mass fraction of the reducing gas. Mass transfer coefficient depends on the intensity of the energy dissipation in the fluid and is evaluated from the correlation by Comiti et al. (2000) as shown in Equation 3:

$$Sh = 3.66 + 0.101\left[1 + \frac{\pi}{4}\frac{1-\varepsilon}{\varepsilon}(\tau - 1)\left(1 + \frac{1}{\tau^2}Sc^{\frac{1}{3}}\exp\left(-\frac{1}{3}\frac{1-\varepsilon}{\varepsilon}\sqrt{\tau Y}Xe_w^{\frac{1}{8}}\right)\right)\right]Xe_w^{\frac{11}{48}}Sc^{\frac{1}{3}} \quad [3]$$

Where *Sh* is Sherwood number, *Sc* is Schmidt number, ε is porosity, Y is particle aspect ratio, Xe_w is wall energetic criterion, and τ is tortuosity.

Schmidt number (*Sc*) is calculated from the ratio of momentum diffusivity to mass diffusivity. Sutherland's law is used to calculate dynamic viscosity as a function of temperature and Sutherland coefficient, and this allows for the evaluation of Sc (Sutherland 1893) . The Sutherland coefficients for H_2O and H_2 are as follows:

H_2: $A_s = 8.76\times10^{-6}$ (kg $m^{-1}s^{-1}K^{-1/2}$) T_s=72 (K)

H_2O: $A_s = 1.12\times10^{-5}$ (kg $m^{-1}s^{-1}K^{-1/2}$) T_s=1064 (K)

Where A_s is Sutherland coefficient and T_s is Sutherland temperature. Dynamic viscosity is calculated as shown in Equation 4.

$$\mu = \frac{A_s\sqrt{T}}{1+\frac{T_s}{T}} \quad \text{(kg } m^{-1}s^{-1}\text{)} \quad [4]$$

Heat of reaction

The energy requirement for the heterogeneous reactions depends on whether the reactions are exothermic or endothermic. The heat of reaction for each reaction step is evaluated from the enthalpy of formation of the species involved in a chemical reaction as shown in Equation 5:

$$\Delta H_r = \sum_i h_f^0, products - \sum_j h_f^0\, reactants \quad [5]$$

Where h_f^0 is the enthalpy of formation at standard conditions. In this study, the prereduction of manganese ore with H_2 is represented by Equations 6 and 7. In this case, the global reactions are used as opposed to the multi-step reactions. This study considers isothermal process at a chosen temperature. The reactions are both exothermic and endothermic and the heat of the reaction is presented in Equation 5. Reaction 6 is exothermic while reaction 7 is endothermic. It should be noted that, although the enthalpy of formation in this section is calculated at standard conditions (1 atm, 298 K), the heat of reaction at the operating temperature in the study was calculated from Equation 17.

$$MnO_{2\,(s)} + H_{2\,(g)} \rightarrow MnO_{(s)} + H_2O_{(g)} \quad \Delta H_r = -376\ kJ/mol \quad [6]$$

$$Fe_2O_{3\,(s)} + 3\,H_{2\,(g)} \rightarrow 2\,Fe_{(s)} + 3\,H_2O_{(g)} \quad \Delta H_r = 582.4\ kJ/mol \quad [7]$$

Governing equations

The governing equations for gas flow through a homogeneous porous medium are presented in Equations 8 to 11, which represent momentum, continuity, species conservation, and energy balance, respectively. In these equations, C_p is the specific heat, ρ represents density, p is pressure, ε is porosity, *u* is fluid velocity, μ_{eff} is the effective viscosity, D_{eff} is the diffusion coefficient, *D* is Darcy's resistance to flow, and *F* is the Forchheimer's term. The superscript *G* refers to gas phase. In Equation 8, a non-Darcy term is included to address the limitations in Darcy's law. Darcy's law is only applicable to creeping flow regimes or low Reynolds number regime, since it neglects the effects of inertial forces on fluid flow and heat transfer (Vafai, Tien, 1981). On the other hand, the Forchheimer model is applicable to flows with Reynolds numbers greater than 10 since, in this regime, the inertial effects are significant. The inertial effects are more pronounced near the boundary and in high porosity media rendering the application of Darcy's law invalid. The Forchheimer model adds the inertial term to the Darcy equation to account for the non-linear behaviour of pressure drop versus flow velocity. The Darcy's equation is presented in Equation 12 while the Forchheimer model is presented in Equation 13.

$$\frac{\partial}{\partial t}\rho^G u + \nabla.(\rho^G uu) + \varepsilon\nabla P - \nabla.\left(\mu_{eff}\nabla u\right) - \rho^G g = -\mu_{eff}\, D.u - F.u \quad [8]$$

$$\frac{\partial}{\partial t}\varepsilon\rho^G + \nabla.(\rho^G u) = (1-\varepsilon)\sum_i R_i^{Reduction} \quad [9]$$

$$\frac{\partial}{\partial t}\varepsilon\rho^G Y_i^G + \nabla\left(\rho^G uY_i^G\right) - \nabla.\left(\varepsilon\rho^G D_{eff}\nabla Y_i^G\right) = \varepsilon w^G + (1-\varepsilon)R_i^{Reduction} \quad [10]$$

$$\frac{\partial(\varepsilon\rho^G Cp^G T^G)}{\partial t} + \nabla.(\rho^G Cp^G T^G u) - \nabla.\nabla\left(\varepsilon k_{eff}^G T^G\right) = -\varepsilon\sum_i w_i h_{f,k}^0 - h_{conv}S_{Av}\left(T^G - T^S\right) + (1-\varepsilon)T^G\sum_i Cp_{,i}\ R_i^{Reduction} + S^{G,Radiation} \quad [11]$$

$$v = -\frac{1}{\mu}K.\nabla P \quad [12]$$

$$\nabla P = \frac{\mu}{K}v - \frac{F\rho}{\sqrt{K}}|v|v \quad [13]$$

The solid phase is described by continuity, species conservation, and energy balance equations as shown in Equation 14 to 16. The solid phase does not include the momentum equation since the particles are immobile. The solid and gas phase interact through the reactions between the gas and solid and heat transfer, and the coupling between the phases is achieved through the reaction rate source term R:

$$\frac{\partial}{\partial t}(1-\varepsilon)\rho^S = (1-\varepsilon)\sum_k R_K^{Reduction} \quad [14]$$

$$\frac{\partial}{\partial t}(1-\varepsilon)Y_k^s\rho^S = (1-\varepsilon)R_K^{Reduction} \quad [15]$$

$$\frac{\partial}{\partial t}(1-\varepsilon)\left(\rho^S C_p^s T^S\right) - \nabla\cdot\left((1-\varepsilon)\mathbb{K}k_{eff}^s\cdot\nabla T^S\right) = h_{conv}S_{Av}(T^G - T^S) + Hr + S^{S,Radiation} \quad [16]$$

$$Hr = (1-\varepsilon)\sum_k h_{f,k}^0 R_k^{Reduction} - (1-\varepsilon)\sum_i Cp_i T^G R_i^{Reduction} \quad [17]$$

Where $R_k^{Reduction}$ denotes reduction rate of solid species and $R_i^{Reduction}$ denotes reduction rate of gas species. The reduction rate is presented in Equation 18:

$$R^{Reduction} = \sum_{k=1}^{ks} v_{i,k} K_{f,i}\rho^s \prod_{j=1}^{Ng+Ns} Y^{v'_{j,k}}, i=1,2,\ldots,N_g+N_s \quad [18]$$

Where $v_{i,k}$ is the stoichiometric coefficient, k_s is the number of elementary reactions, N_g is the number of gas phase species, and N_s is the number of solid phase species. K_f is the rate constant and $v'_{j,k}$ is reaction order. The rate constant depends on temperature and is described by Equation 19:

$$K_f = Aexp(-\frac{Ta}{T}) \quad [19]$$

Where T_a is the activation temperature and A is the pre-exponential factor.

Initial and boundary conditions

At the inlet boundary condition, temperature, velocity and composition of gas (Y_i^G), and solid (Y_k^s) are known. A no slip boundary condition is imposed for velocity at the walls and at the inlet, gas velocity is specified. The reactions take place at the ore surface, and the boundary condition at the interface is described by Equation 20. At the outlet boundary, heat flux and mass flux are assumed to be zero as shown in Equation 21 to 22. The heat and mass flux are assumed to be zero at the outlet because the flow is assumed to be fully developed. The flow regime is laminar and the assumption of a fully developed flow for shorter domains is valid. A summary of initial and boundary conditions is presented in Table 1.

$$\rho D_{eff}\nabla Y_k^s = R_k^s \quad [20]$$

$$\nabla T_G|_{outlet} = 0 \quad [21]$$

$$\nabla Y_i^G|_{outlet} = 0 \quad [22]$$

The convective heat transfer at the interface is defined by Equation 23:

$$q = S_{AV}h(T_g - T_s) \quad [23]$$

Where S_{AV} denotes the surface area to volume ratio, h is the convective heat transfer coefficient, T_g the gas phase temperature, and T_s is the solid phase temperature.

Geometry and meshing

The dimensions of a shaft furnace considered in the study are presented in Table 2. Gmsh mesh generator was used to generate the mesh for a 3D and 2D axisymmetric geometry as presented in Figure 2. The manganese particles are packed in the furnace from 1.2 m to 1.85 m as observed in Figure 2. The porous medium is

Table 1

A summary of initial and boundary conditions

Initial condition		Boundary conditions		
		Inlet	Outlet	Walls
Volumetric flowrate	0 l/min	100 l/min	zero gradient	0 l/min
Pressure	101300 Pa	zero gradient	101300 Pa	zero gradient
Temperature (solid phase)	800°C	zero gradient	zero gradient	zero gradient
Temperature (gas phase)	800°C	800°C	zero gradient	zero gradient

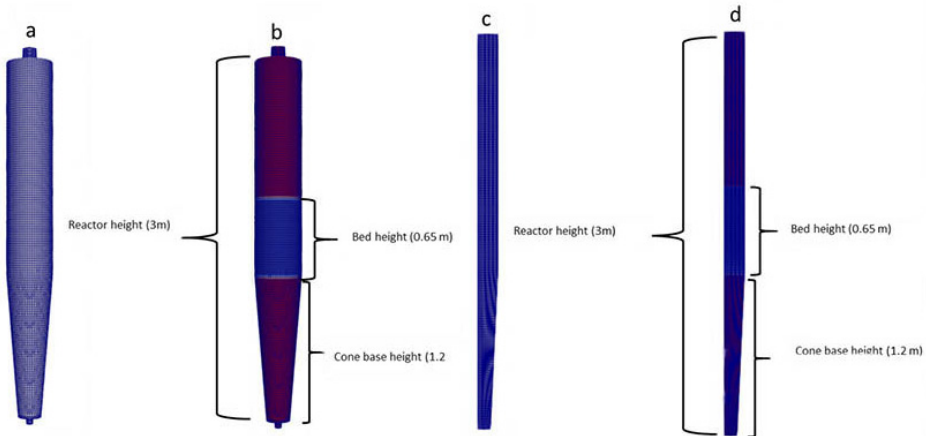

Figure 1—A graphical representation of the shaft furnace with a porosity field. 3D geometry (a) and associated dimensions (b), 2D-axisysmetry geometry (c) and associated dimensions (d)

Table 2

Reactor dimensions and operating conditions

Reactor height (m)	3.00
Reactor diameter (m)	0.39
Cone height (m)	1.20
Cone base diameter (m)	0.20
Inlet diameter (m)	0.06
Outlet diameter (m)	0.12
Bed height (m)	0.65
Initial bed porosity	0.25
Inlet H_2 mass fraction	0.95
Inlet N_2 mass fraction	0.05
Inlet gas flow rate (l/min)	100
MnO_2 initial mass fraction	0.82
Fe_2O_3 initial mass fraction	0.18

usually inhomogeneous however, it was assumed that porosity is uniformly distributed through a bed of particles.

Mesh sensitivity analysis

A solution approach to any numerical problem must achieve convergence, consistency, and numerical stability in order to be considered accurate. The criterion for convergence is a close agreement between the numerical solution and the exact solution as grid spacing tends to zero. In the current work, mesh sensitivity analysis on the 2D-axisymetric model was undertaken and the results are presented in Figure 2. The species mass fraction profiles at various grid sizes reveal that at grid 1, the mass fraction profiles are resolution dependent. Refining the mesh size to grid sizes larger than grid 2 resulted in no difference in the predicted mass fraction, thus revealing grid 2 as the optimum mesh size. The number of cells in Grid 1, Grid 2, and Grid 3 is 5 241, 10 482, and 31 446, respectively. For the 3D geometry, the number of cells in Grid 1, Grid 2 and Grid 3 is 23 807, 47 614, and 71 421, respectively.

Results and discussions

The computational solution to Navier-Stokes and transport equations was carried out in OpenFOAM® 8. The coupling of chemistry and transport processes was done by using the OpenFOAM® solver for heterogeneous reacting flows developed by Jan Źuk et al. (2022). These authors developed their framework at the top of OpenFOAM® wherein the mesh and discretisation of Navier-Stokes equations is managed through the OpenFOAM® framework, while their CFD code focused on the reaction mechanisms and gas-solid reactions as the reducing gas flows through the porous medium.

This study investigates prereduction in a shaft furnace with the dimensions and operating conditions shown in Table 2. A 2D-axisymetric and a 3D model results are compared to investigate whether their predictions are similar. 2D-axisymetric models are not computationally expensive when compared to 3D models, and if their predictions are found to be viable, this will result in faster evaluation of shaft furnace performance indicators. However, the inability to predict asymmetry of flow patterns and transversal fluid flow constitute some limitations inherent to 2D-axisymmetric models (Mezhericher et al., 2009). The mass fraction profiles for a 3D geometry are presented in Figures 3 to 6. The mass fraction profiles of reactants and products indicate that at 2450 seconds (40.8 minutes), reduction is complete. At 1100 seconds (18.3 minutes), only a fraction of the 0.65 m bed height is reduced, and this indicates that mass transfer controls the rate of reduction. To circumvent this limitation, the flowrate of the H_2 needs to be increased. The increase in the reducing gas flow rate results in the

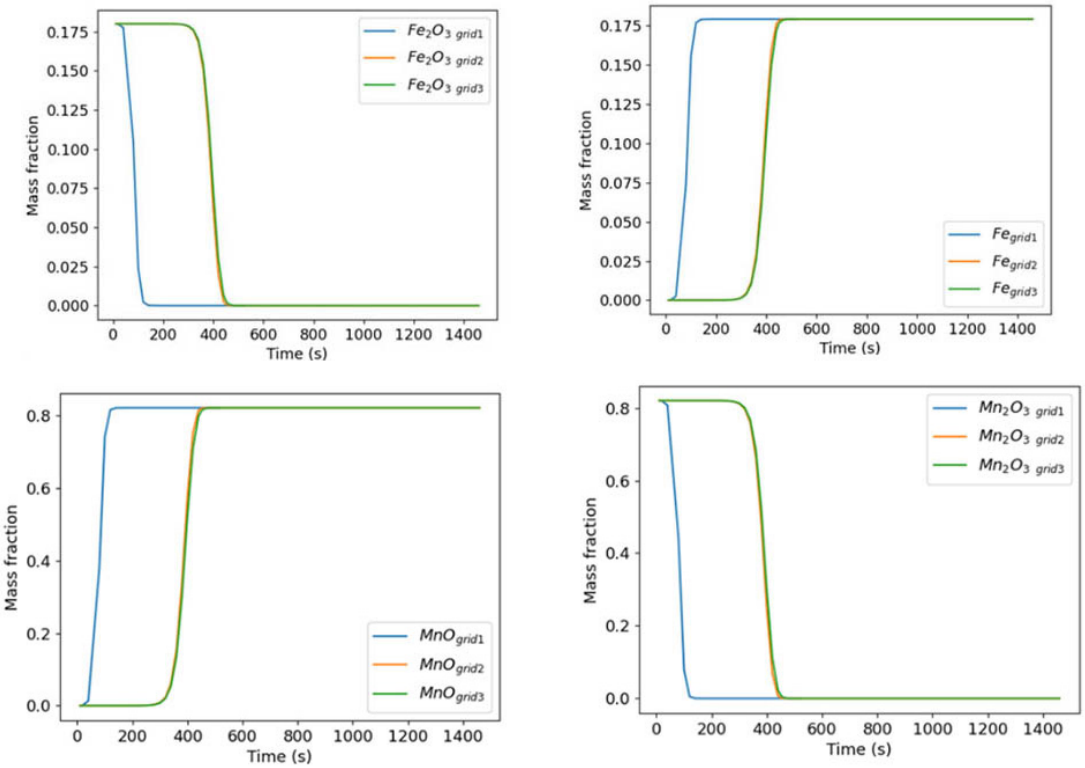

Figure 2—Species mass fraction profiles at different mesh sizes

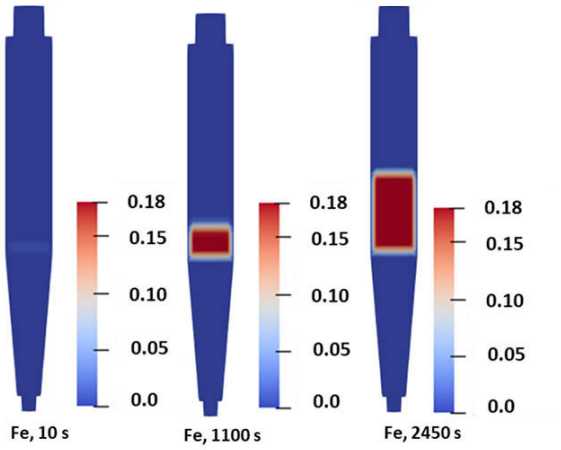

Figure 3—Fe mass fraction profiles

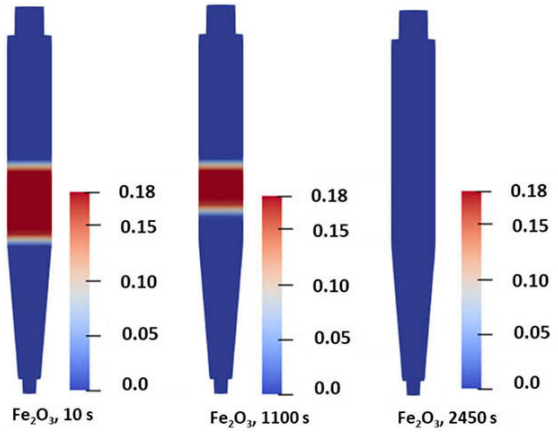

Figure 4—Fe_2O_3 mass fraction profiles

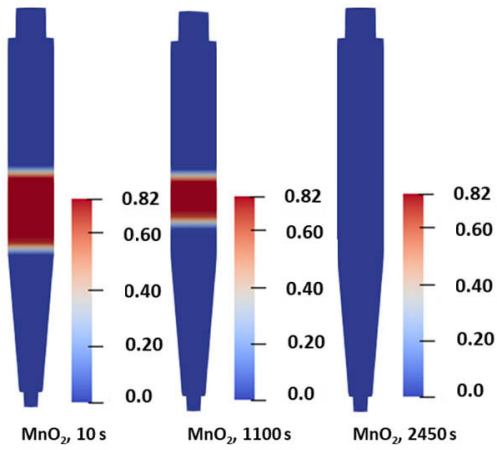

Figure 5—MnO_2 mass fraction profiles

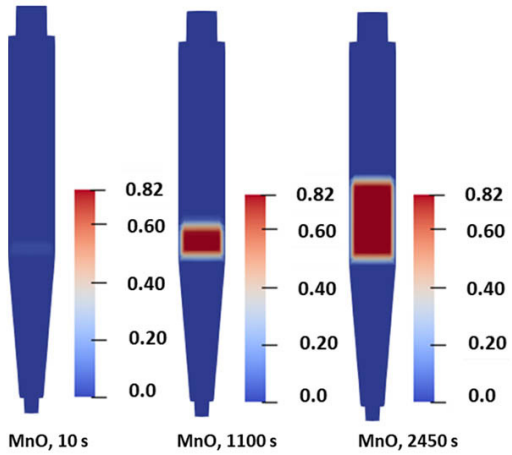

Figure 6—MnO mass fraction profiles

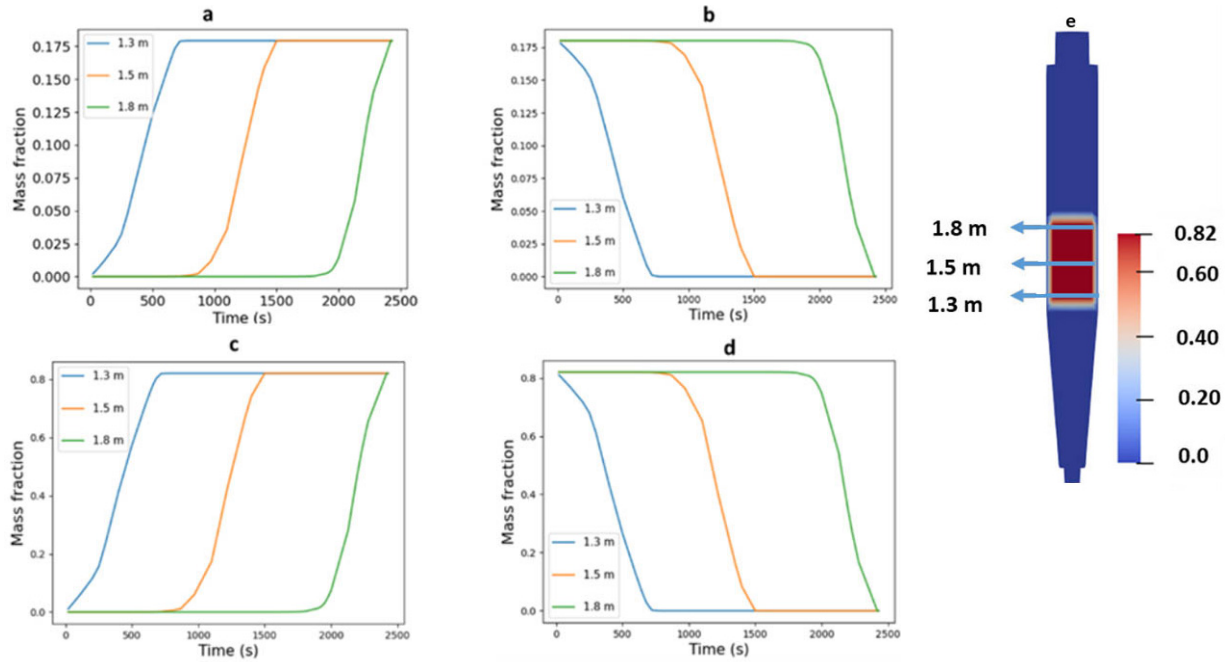

Figure 7—Species mass fraction profiles at various compartments a) Fe, b) Fe_2O_3, c) MnO, d) MnO_2, and e) representation of the compartments

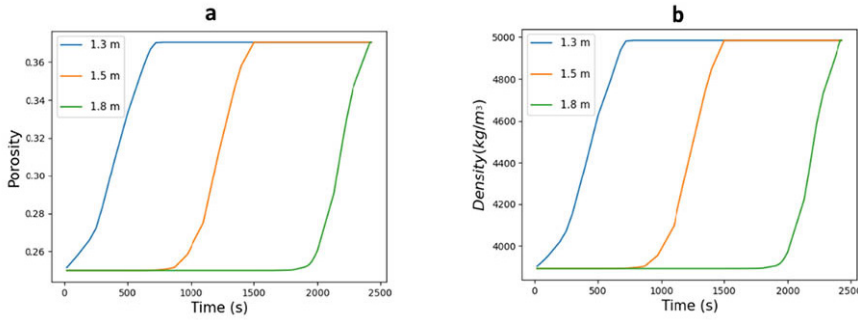

Figure 8—Porosity (a) and density (b) profiles

increased diffusion through the boundary layer, and as a result, an increased rate of reduction. Increasing H_2 partial pressure increases the rate of adsorption, which ultimately results in an increased rate of reduction. In order to elucidate the spatial distribution of the rate of reduction, the shaft furnace was compartmentalised and the mass fraction profiles at each compartment are shown in Figure 7.

The species mass fraction profiles at 1.3 m, 1.5 m, and 1.8 m are shown in Figure 7. A total mass balance was performed as a way to gauge whether the model is consistent in its predictions. The consistency tests on each compartment reveal that the mass balance is closed. The mass fraction results show that at 1.3 m, the reduction to metallic iron and MnO is complete at 500 seconds (8,33 minutes), while the reduction at 1.8 mm is complete at 2450 seconds (40,83 minutes). This is attributed to the effects of mass transfer limitations more pronounced at longer bed heights.

A change in particle density and porosity as products are formed, is presented in Figure 8. Formation of products results in the particle density changes and subsequently changes in porosity. Generally, the increase in bulk density at constant particle density results in the decrease in porosity (Kurgan, 2014). However, in this study, particle density increases as metallic iron and MnO are formed from reduction reactions and, given that the total mass does not change, porosity is expected to increase. The results in Figure 8 show that a change in porosity and the density is rapid on the lower section of the particles' bed because the lower compartment is the first point of contact with the reducing gas. It is crucial that a CFD model predicts structural changes during the phase transformation. This is important because the formation of intermediate products may result in the formation of dense phase with low porosity, thus blocking the access of reducing gases to the reaction interface.

Chemical reactions and diffusion normally play a role in controlling the rate of reactions. If chemical reactions are slow, the rate of reactions are controlled by chemical reactions and, if diffusion is slow, the process is diffusion controlled. In this study, Equation 24 is used to determine the operating regime. The equation evaluates the fraction of diffusion flux and, whenever the fraction is less than 0.5, it can be concluded that diffusion is slower than chemical reactions. As observed in Figure 9, when the reducing gas reaches a compartment of interest, the diffusion flux fraction is always less than 0.5, indicating that diffusion is rate limiting. When reduction is complete or not yet started, the fraction of diffusive flux is unity as the reaction rate flux is zero.

The rate of H_2 transport from the bulk phase to reaction sites influences the reaction concentration, and owing to this, the analysis of the effect of diffusion and convection is performed. Péclet number (*Pe*) is used to determine the effect of diffusion and advection. *Pe* is defined as shown in Equation 25. The results in Figure 10 reveal that convective transport contributes significantly towards overall mass transport because Pe is always greater than unity. The results indicate that the effect of axial dispersion is insignificant.

$$Diffusive\ flux_{fraction} = \frac{J''}{J''+R''} \quad [24]$$

Where J''(kg m^{-3} s^{-1}) is the diffusion flux and R''(kg m^{-3} s^{-1}) is the reaction rate flux.

Pe = (convection transport)/(diffusion transport)

$$Pe = \frac{convection\ transport}{diffusion\ transport} \quad [25]$$

2D-axisymetric model results

The mass fraction profiles predicted from a 2D-axisymetric model are presented in Figures 11 to 14. Similar to the 3D model, the reactor is compartmentalised to allow for the description of the spatial distribution of mass fraction profiles. In this case, the reduction is complete in all compartments at 600 seconds (10 Minutes), while the 3D model results in complete reduction at 2450 seconds (40,83 minutes). Therefore, the computational accuracy of the two models is different and for a more accurate description of prereduction behaviour in a shaft furnace, a 3D model should

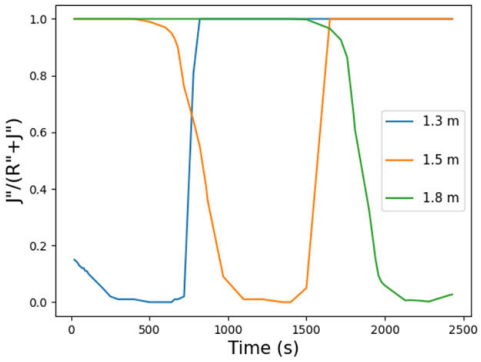

Figure 9—Fraction of diffusive flux (where *J"* is the diffusive flux and *R"* is the reaction rate flux)

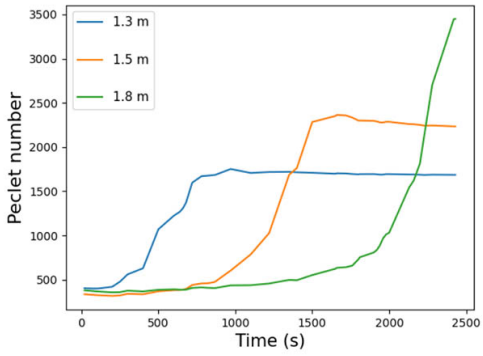

Figure 10—Péclet number profile

be used. Although the 2D-axisymetric model overestimates the reaction rates, the manifestation of mass transfer limitations is still as apparent as in the 3D model. The 3D model results were validated against experimental results already presented, therefore, it is postulated that the 2D-axisymetric model overestimates the reaction rates.

The effect of H_2 flowrate on the rate of prereduction was investigated, and the results are presented in Figure 15. As observed, the higher H_2 flowrates result in an increased rate of reduction. This is because an increase in the reducing gas flow rate leads to increased diffusion through the boundary layer, as a result an increased rate of reduction.

Model validation

There are no experimental data for prereduction of manganese in a shaft furnace, however, there are experimental data for prereduction in a thermogravimetric analysis furnace (TGA). Therefore, to validate the predictions of the CFD model, experimental percentage mass loss data from the TGA were used. In this case, the CFD model was used to predict the prereduction behaviour of manganese under H_2 reducing atmosphere in a TGA furnace. The CFD predictions for a TGA furnace were compared with the experimental measurements from the TGA by Sarkar et al. (2023). The results presented in Figure 15 concern prereduction in the TGA with 4.5 cm diameter and 48 cm in height at 700°C at the H_2 flow rate of 4 l/min. As observed, there is a close agreement between experimental and model percentage mass loss data up to 2500 seconds (41,66 minutes), and thereafter a discrepancy is observed with a maximum error of 1%. The discrepancy can be attributed to the decomposition of carbonates in the experimental measurements, which results in CO_2 evolution and increased mass loss. On the other hand, the CFD model only describes mass loss from reduction reactions and does not take into account mass loss due to carbonate decomposition.

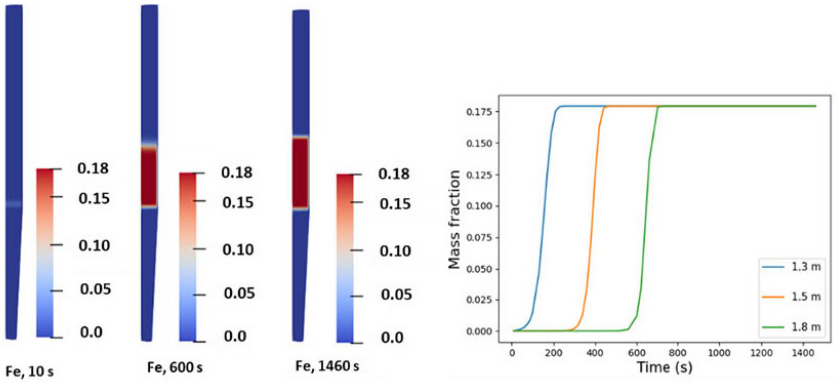

Figure 11—Fe mass fraction profiles

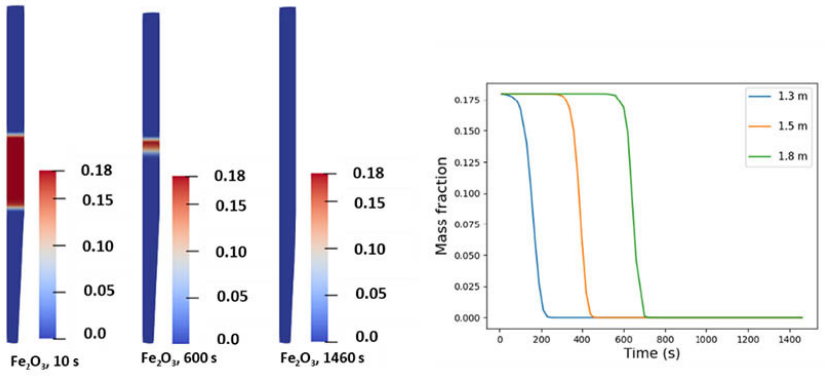

Figure 12—Fe_2O_3 mass fraction profiles

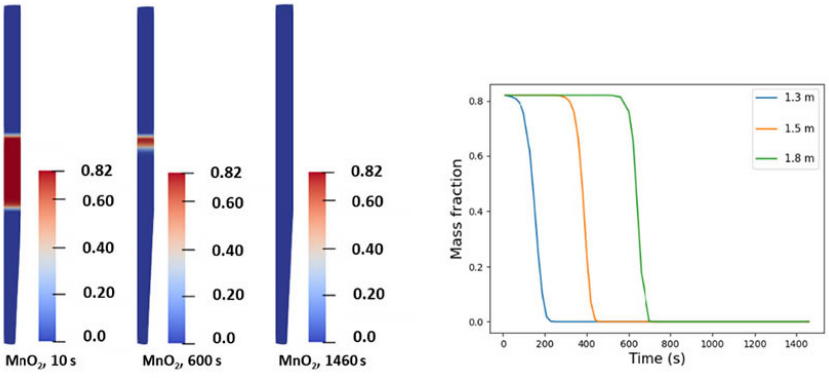

Figure 13—MnO_2 mass fraction profiles

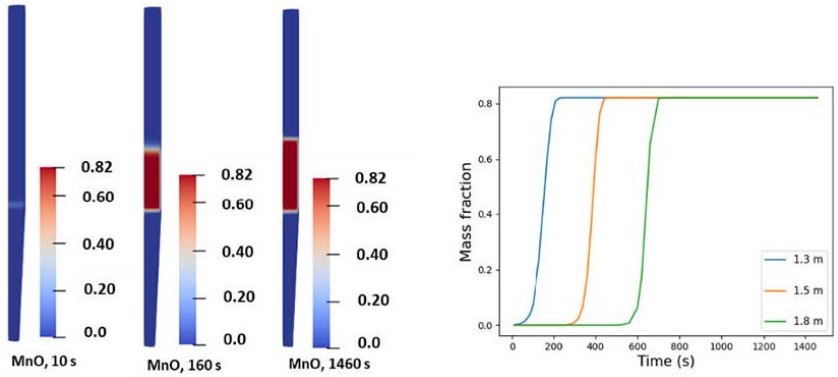

Figure 14—MnO mass fraction profiles

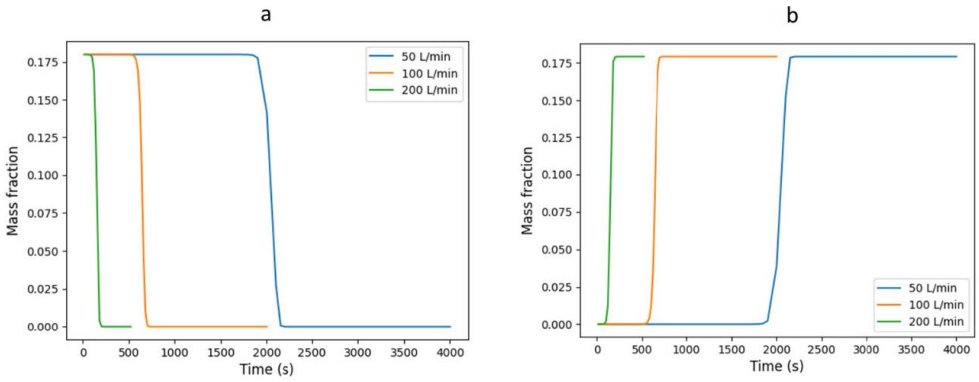

Figure 15—Species mass fraction profiles at various H_2 flowrates a) Fe_2O_3 and b) Fe

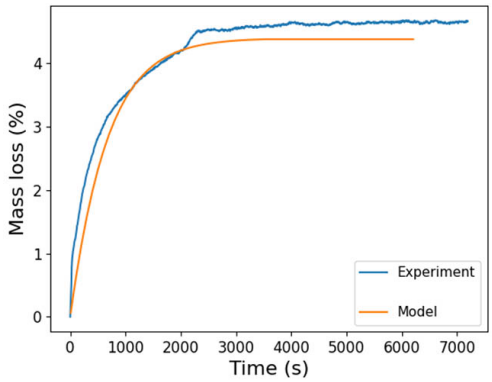

Figure 16—Percentage mass loss data from experimental measurements and model predictions

Conclusions

The CFD modelling of prereduction of manganese ore in a shaft furnace has demonstrated that longer bed heights require high H2 flowrate to facilitate faster rates of reduction. At low flowrates and long bed heights, the effect of diffusion limitations on the reactions is more pronounced. This is attributed to a long boundary layer thickness at low gas flowrates and slower rates of mass transfer. The computational accuracy of the 2D-axisymmetric and the 3D model is different and this results in the overestimation of the rate of reduction in the 2D-axisymmetric case. The 3D models are required to predict the dynamic features of a shaft furnace and evaluate performance indicators. The CFD models are able to predict whether mass transfer or kinetics control the reaction rates and this is crucial in the design and optimisation of heterogeneous reactors. However, the CFD model does not include the effects of sintering and future work will incorporate this. Sintering has a retarding effect on reduction since it results in the blockage of pores, thus hindering the transport of reducing gases to the reaction sites. Future work will incorporate sintering by utilising discrete element method (DEM) and assigning to particles models such as inter-particle bond formation, grain coalescence models, breakage models, heat transfer models, contact models, and consideration of mass transport due to surface and grain boundary diffusion. Currently, the models assume homogeneous porous medium, however, in the future, the inhomogeneity of the porous medium will be captured by considering a non-uniform porosity distribution, and a micro CT based method will be used to validate porosity of prereduced product predicted by the CFD model.

Notation

T_s	solid phase temperature	K
T_g	gas phase temperature	K
C_p	specific heat	J $kg^{-1}K^{-1}$
Da	Damkohler number, dimensionless	
K_g	mass transfer coefficient	ms^{-1}
R^{dif}_s	volume averaged reaction rate	kg $m^{-3}s^{-1}$
ρ^G	gas density	kg m^{-3}
Y_i^G	bulk mass fraction of the reduction gas, dimensionless	
Y_i^s	surface mass fraction of the reducing gas, dimensionless	
Sh	Sherwood number, dimensionless	
Sc	Schmidt number, dimensionless	
Y	particle aspect ratio, dimensionless	
Xe_w	wall energetic criterion, dimensionless	
τ	tortuosity, dimensionless	
A_s	Sutherland coefficient	kg $m^{-1}s^{-1}K^{-1/2}$

T_s	Sutherland temperature	.....K
μ	dynamic viscosity	.....kg $m^{-1}s^{-1}$
h_f^0	enthalpy of formation	..... kJ mol^{-1}
p	pressure	..... Pa
u	fluid velocity	.....m s^{-1}
D	Darcy's resistance to flow	..... m^{-2}
$R_k^{Reduction}$	reduction rate of solid phase species	.....kg $m^{-3}s^{-1}$
$R_i^{Reduction}$	reduction rate of gas phase species	.....kg $m^{-3}s^{-1}$
A	pre-exponential factor	..... s^{-1}
T_a	activation temperature	.....K
Pe	Péclet number, dimensionless	

Acknowledgments

This paper is published with the permission of Mintek. The authors acknowledge the Centre for High Performance Computing (CHPC), South Africa, for providing computational resources to this research project. The authors are grateful to Mintek (PDR-24023) and HAlMan (PDE-23002) for financial support.
Conflicts of Interest: The authors declare no conflict of interest

References

Ahn, Hyungjun, Sangmin Choi. 2017. "A Comparison of the Shrinking Core Model and the Grain Model for the Iron Ore Pellet Indurator Simulation." *Computers and Chemical Engineering,* vol. 97, pp.13–26. doi: 10.1016/j.compchemeng.2016.11.005.

Christmann, K. 1988. *Interaction Of Hydrogen With Solid Surfaces*. Vol. 9. Armsterdam.

Coetsee, T., Reinke, C., Nell, J., Pistorius, P.J. 2015. "Reduction Mechanisms in Manganese Ore Reduction." *Metallurgical and Materials Transactions B: Process Metallurgy and Materials Processing Science,* vol. 46, no. 6 pp. 2534–52. doi: 10.1007/s11663-015-0414-y.

Comiti, J.,Mauret, E., Renaud, M. 2000. "Mass Transfer in Fixed Beds: Proposition of a Generalized Correlation Based on an Energetic Criterion." *Chemical Engineering Science,* vol. 55, pp. 5545–54.

Davies, J., Tangstad, M., Schanche, T.L., Du Preez. S.P. 2023. "Pre-Reduction of United Manganese of Kalahari Ore in CO/CO2, H2/H2O, and H2 Atmospheres." *Metallurgical and Materials Transactions B,* vol. 54, no. 2 pp. 515–35. doi: 10.1007/s11663-022-02705-0

Fei, Yang., Guan, X., Kuang, S., Yu, A., Yang, N. 2024. "A Review on the Modeling and Simulation of Shaft Furnace Hydrogen Metallurgy: A Chemical Engineering Perspective." *ACS Engineering Au,* vol. 4, no. 2, pp. 45–65. doi: 10.1021/acsengineeringau.3c00033

Hamadeh, H., Mirgaux, O., Patisson, F. 2018. "Detailed Modeling of the Direct Reduction of Iron Ore in a Shaft Furnace." *Materials, vol.* 11, no. 10. doi: 10.3390/ma11101865

Jan Źuk, Pawel, Bartosz Tuźnik, Tadeusz Rymarz, Kamil Kwiatkowski, Marek Dudynski, Flavio C. C. Galeazzo, and Guenther C. Krieger. 2022. "OpenFOAM Solver for Thermal and Chemical Conversion in Porous." *Computers and Physics Communications,* vol. 278, no. 1–19. doi: 10.1016/j.cpc.2022.108407

Kinaci, M.E., Lichtenegger, T., Schneiderbauer, S. 2020. "A CFD-DEM Model for the Simulation of Direct Reduction of Iron-Ore in Fluidized Beds." *Chemical Engineering Science, vol.* 227. doi: 10.1016/j.ces.2020.115858.

Kung, H.H. 1989. Transition Metal Oxides: *Surface Chemistry and Catalysis*. vol. 45. 1st ed.

Kurgan, N. 2014. "Effect of Porosity and Density on the Mechanical and Microstructural Properties of Sintered 316L Stainless Steel Implant Materials." *Materials and Design,* vol. 55, pp. 235–41. doi: 10.1016/j.matdes.2013.09.058.

Li, Q., Ghadiani, H.,Jalilvand, V., Alam, T., Farhat, Z., Aminul Islam, Md. 2024. "Hydrogen Impact: A Review on Diffusibility, Embrittlement Mechanisms, and Characterization." *Materials,* vol. 17, no. 4.

Liu, W., Zhu, D., Pan, J., Wei, Z., Yang, C., Guo, Z., Zhang, W., Ruan, Z., Jiang, L. 2024. "Study on Sintering Technology of Manganese Ore Fines Strengthened by Pellet-Sintering Process." *Journal of Sustainable Metallurgy,* vol. 10, no. 3 pp. 1415–27. doi: 10.1007/s40831-024-00866-7

Liu, Z., Lu, S., Wang, Y., Zhang, J., Cheng, Q., Ma, Y. 2023. "Study on Optimization of Reduction Temperature of Hydrogen-Based Shaft Furnace—Numerical Simulation and Multi-Criteria Evaluation." *International Journal of Hydrogen Energy,* vol. 48, no. 42, pp.16132–42. doi: 10.1016/j.ijhydene.2023.01.057

Li, Z., Qi, Z., Zhang, L.,Guo, M.,Liang, D., Dong, Q. 2023. "Numerical Simulation of H2-Intensive Shaft Furnace Direct Reduction Process." *Journal of Cleaner Production,* vol. 409. doi: 10.1016/j.jclepro.2023.137059

Ma, Y., Isnaldi R., Souza F., Yang, B., Schenk, J., Patisson, F., Beck, A., Jeroen, A., Van Bokhoven, M., Willinger, G., Li, K., Xie, D., Ponge, D., Zaefferer, S., Baptiste, G., Jaber, R., Mianroodi, Raabe, D. 2022. "Hierarchical Nature of Hydrogen-Based Direct Reduction of Iron Oxides." *Scripta Materialia*, vol. 213. doi: 10.1016/j.scriptamat.2022.114571

Mezhericher, M., Levy, A., Borde, I. 2009. "Modeling of Droplet Drying in Spray Chambers Using 2D and 3D Computational Fluid Dynamics." *Drying Technology9, vol.* 27, no. 3, pp. 359–70. doi: 10.1080/07373930802682940

Patisson, F., Mirgaux, O. 2020. "Hydrogen Ironmaking: How It Works." *Metals,* vol. 10, no. 7, pp. 1–15. doi: 10.3390/met10070922

Rukini, A., Rhamdhani, M.A., Brooks, G.A., Van den Bulck, A. 2022. "Metals Production and Metal Oxides Reduction Using Hydrogen: A Review." *Journal of Sustainable Metallurgy,* vol. 8, no. 1.

Sarkar, A., Schanche, T.L.,Jafar Safarian, J. 2023. "Isothermal Pre-Reduction Behavior of Nchwaning Manganese Ore in H2 Atmosphere." Pp. 2–9 in *Material Proceedings*. MDPI AG.

Vafai, K., Tien, C.L. 1981. "Boundary And Inertia Effects On Flow And Heat Transfer In Porous Media." I*nternational Journal of Heat and Mass Transfer,* vol. 24, pp. 195–203.

Wesenauer, F., Jordan, C., Pichler, M., Frei, A., Azam, M., Jahromy, S.S., Harasek, M., Winter, F. 2020. "An Unreacted Shrinking Core Model Serves for Predicting Combustion Rates of Organic Additives in Clay Bricks." *Energy and Fuels,* vol. 34, no. 12, pp. 16679–92. doi: 10.1021/acs.energyfuels.0c03075

Wu, S., Zhang, Y., Li, H., Zhang, S., Kasai, E., Wang, C. 2024. "Hydrogen-Based Pre-Reduction of Chromite: Reduction and Consolidation Mechanisms." *International Journal of Hydrogen Energy,* vol. 50, pp. 397–410. doi: 10.1016/j.ijhydene.2023.09.026 ◆